Dynamics of Chiral Fermions in Condensed Matter Systems*

Qiang Li
Department of Physics and Astronomy, Stony Brook University,
Stony Brook, NY 11794-3800, USA
Condensed Matter Physics & Materials Science Division, Brookhaven National Laboratory,
Upton, New York 11973-5000, USA
E-mail: qiang.li@stonybrook.edu, or qiangli@bnl.gov
www.stonybrook.edu, www.bnl.gov

In condensed matters, such as 3D Dirac and Weyl semimetals, fermions with linear energy-momentum dispersion gain chirality (handedness). The chiral anomaly produces an imbalance between the densities of right- and left-handed fermions, leading to generation of electric current in parallel electric and magnetic fields. This is called the chiral magnetic effect. Coupling of circular polarized light to chiral fermions breaks the chiral symmetry, and can generate chirality-dependent photocurrent. In this article, we review dynamics of chiral fermions in condensed matter systems to explain the theory of chiral magnetic effect and describe experimental signatures of the chiral anomaly. We then summarize recent theoretical and experimental studies of topological phase transition involving Dirac and Weyl semimetals, and detections of chirality and chiral photocurrent in static and dynamically-driven Weyl states. We conclude with potential uses of chiral fermions in quantum information systems

Keywords: Chiral Fermions; Chiral Anomaly; Chiral Magnetic Effect; Dirac and Weyl Semimetals

1. Introduction

The last decade has seen a dramatic shift in the focus of condensed matter physics. Topology has emerged as an organizing principle of states of matter that transcends the conventional classification in terms of phase transitions and symmetry breaking, as expressed in Landau's theory. A unique feature that makes many topological materials' electronic properties different from all other condensed matter systems is the linear dispersion of their low-energy excitations. This has led to a fascinating convergence between condensed matter physics and high energy nuclear physics.

Massless Dirac particles having linear energy-momentum dispersion are described by the Dirac equation $\hat{H} = c\vec{\sigma} \cdot \hat{p}$, where c is the speed of light, $\vec{\sigma}$ is the Pauli matrix, and $\hat{p}$ is the momentum operator. In condensed matters, linear dispersion makes electrons near the Fermi energy behave like massless Dirac fermions, which is different from all other condensed matter systems described by the non-relativistic Schrödinger equation and quadratic dispersion of electrons – $\hat{H} = \hat{p}^2/2m^*$, where m^* is the effective mass [1]. To describe linear dispersion in condensed matter systems, an analog to the Dirac equation is used, where the speed of the light is replaced by the Fermi-velocity of the quasi-particles [1].

---

*This work is supported by the U.S. Department of Energy, Office of Basic Energy Sciences, Division of Materials Sciences and Engineering, under Contract No. DE-SC0012704.

Materials having states with linear dispersion include graphene [2, 3], topological insulators [4, 5], and Dirac and Weyl semimetals [6–9].

Topological insulators (TI, e.g., HgTe and Bi_2Se_3) display the intriguing property of being insulating in the bulk but conducting on the surface [4, 5]. This feature is enabled by Dirac-like surface states that arise from strong spin-orbit coupling. The spin in these topological states is locked at a right angle to the charge carriers' momentum. Closely related to TIs are topological semimetals, such as *Dirac semimetals* (DSM e.g., Na_3Bi,Cd_3As_2) and *Weyl semimetals* (WSM, e.g., TaAs) [6–11], which are three dimensional (3D) analogs of graphene. The bulk states – gapless fermions – in 3D topological semimetals are described by eigenstates of the Weyl or Dirac equation with a definite projection of spin onto momentum. This fermion is right-handed (parallel) or left-handed (anti-parallel), dictated by relativistic quantum field theory for a system with even spacetime dimension. This "handedness" is called chirality and is depicted in Fig. 1b, along with a description of chiral materials such as DSMs and WSMs (Fig. 1a), a schematic of the chiral anomaly (Fig. 1d), and examples of chiral applications (Fig. 1c, 1e, 1f).

In this article, we review dynamics of chiral fermions in condensed matters, a rapidly developing field. We begin in Sec. 2 with an introduction to the chiral

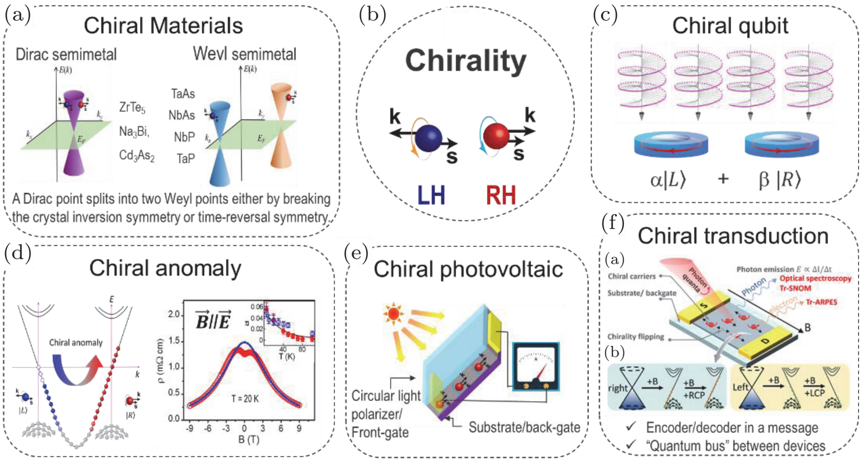

Fig. 1. Chiral fermions in condensed matter systems: (a) A Dirac semimetal (purple) hosts both left-handed (L)-and right-handed (R)-fermions on the same band. A Weyl semimetal (blue and orange) hosts L-and R-fermions on separate bands. (b) The definition of chirality in relativistic quantum field theory. (c) Chiral qubits have two base states describing chiral fermions circulating clockwise and counter-clockwise [13]. (d) The chiral anomaly is manifested, e.g., as the chiral magnetic effect, generation of an electric current by external gauge fields with non-trivial topology (e.g. by parallel electric and magnetic fields). The signature of the chiral magnetic effect is the negative longitudinal magnetoresistance discovered in the Dirac semimetal $ZrTe_5$ [12]. (e) The chiral photovoltaic cell enables a production of electric current in a Weyl semimetal via circular photogalvanic effect. (f) Chiral transduction uses chirality as an encoder/decoder in transmitting a message and serves as a "quantum bus" between quantum devices operating at different frequencies.

magnetic effect and chiral anomaly. Sec. 3 describes the topological phase transitions between TIs and DSMs/WSMs and discusses the static and dynamic controls of the band topology transition. Sec. 4 describes chiral photocurrent generation and discusses potential uses of chiral fermions for quantum information science and technology.

2. Chiral magnetic effect and chiral anomaly

The conservation of chiral symmetry implies that populations of right- and left-handed massless fermions are separately conserved. However, coupling of the fermions to a vector gauge potential breaks the chiral symmetry, leading to the appearance of a chiral anomaly. The chiral anomaly was discovered in 1969 based on the observation of the rapid decay of the neutral pion π^0 into photons [14]. In 1983, Nielsen and Ninomiya pointed out a similarity between the fermion system of lattice gauge theories and the electron system of gapless semiconductors, in which energy bands have point-like degeneracy [16], known now as Weyl semimetals (WSM). Nielsen and Ninomiya predicted that longitudinal magnetoconductivity becomes large for Weyl fermions in parallel electric and magnetic fields.

In relativistic heavy-ion collisions, the chiral anomaly manifests as the chiral magnetic effect that transforms the chiral asymmetry, generated by topological transitions in hot QCD matter, into an electric current, where magnetic field is produced by the colliding ions. The chiral magnetic effect in hot QCD matter was first predicted by Kharzeev and colleagues [17] and since has been intensely studied in heavy ion collision experiments at Relativistic Heavy Ion Collider (RHIC) at BNL and the Large Hadron Collider (LHC) at CERN [18]. Of note, when chiral asymmetry is produced by parallel electric and magnetic fields, either in condensed matters (e.g., WSMs) or in quark gluon plasmas, the chiral anomaly and the chiral magnetic effect describe the same phenomenon. Here, we will use the terms interchangeably.

The recent experimental discovery of DSM/WSM has opened unprecedented opportunities to study the quantum dynamics of relativistic field theory in condensed matter systems. The chiral magnetic effect was discovered experimentally in the DSM $ZrTe_5$ by the author and collaborators [12] in 2014. Below, we explain the chiral magnetic effect using a DSM $ZrTe_5$ as an example.

In the absence of external fields, each Dirac point contains left- and right-handed fermions with equal chemical potentials, $\mu_L = \mu_R = 0$. Applying a magnetic field breaks time reversal symmetry that can transform a DSM into a WSM. If the energy degeneracy between the left- and right-handed fermions is broken, quantum electrodynamics dictate that the parallel external electric and magnetic fields will generate the chiral charge ρ_5 with the rate given by

$$\frac{d\rho_5}{dt} = \frac{e^2}{4\pi^2\hbar^2 c}\vec{E}\cdot\vec{B}. \tag{1}$$

The ρ_5 is controlled by the chiral chemical potential $\mu_5 \equiv (\mu_R - \mu_L)/2$ and given by [17]

$$\rho_5 = \frac{\mu_5^3}{3\pi^2 v^2} + \frac{\mu_5}{3v^3}\left(T^2 + \frac{\mu^2}{\pi^2}\right), \tag{2}$$

where $\mu = (\mu_R + \mu_L)/2$, and v is the Fermi velocity. The left- and right-handed fermions in chiral matters can mix through chirality-changing scattering. Introducing the chirality-changing scattering time τ_{V}, we thus get the equation

$$\frac{d\rho_5}{dt} = \frac{e^2}{4\pi^2\hbar^2 c}\vec{E}\cdot\vec{B} - \frac{\rho_5}{\tau_V}. \tag{3}$$

The solution of equation (3) at $t >> \tau_{\mathrm{V}}$ is

$$\rho_5 = \frac{e^2}{4\pi^2\hbar^2 c}\vec{E}\cdot\vec{B}\tau_V. \tag{4}$$

Assuming that $\mu_5 << \mu$, T, we obtain the non-zero chiral chemical potential μ_5 as

$$\mu_5 = \frac{3}{4}\frac{v^3}{\pi^2}\frac{e^2}{\hbar^2 c}\frac{\vec{E}\cdot\vec{B}}{T^2 + \frac{\mu^2}{\pi^2}}\tau_V. \tag{5}$$

The corresponding chiral magnetic current can be computed [17] and is given by

$$\vec{J}_{\mathrm{CME}} = \frac{e^2}{2\pi^2}\mu_5\vec{B} = \sigma_{\mathrm{CME}}\vec{E}. \tag{6}$$

When the electric and magnetic fields are parallel, the CME conductivity is given by

$$\sigma_{\mathrm{CME}} = \frac{e^2}{\pi\hbar}\frac{3}{8}\frac{e^2}{\hbar c}\frac{v^3}{\pi^3}\frac{\tau_V}{T^2 + \frac{\mu^2}{\pi^2}}B^2. \tag{7}$$

Magnetoconductance σ_{CME} induced by the chiral magnetic effect has a characteristic quadratic dependence on magnetic field in weak field limits. It is precisely this dependence of longitudinal magnetoconductance that was observed in $\mathrm{ZrTe_5}$ (Fig. 2d) [12]. Fig. 2a, 2b, and 2c show the linearly dispersed electronic bands near Fermi level, the measurement configuration, and the orientation dependence of magnetoresistance, respectively. In this experiment, the current and voltage contacts on the single crystal $\mathrm{ZrTe_5}$ (Fig. 2b) provided a uniform flow of electric current and uniform voltage detection. Thus, the data is free of measurement artifacts such as the current-jetting found in other measurements [19]. The chiral anomaly was also detected in another DSM $\mathrm{Na_3Bi}$ in 2015, then subsequently in a dozen more materials, including WSM TaP [20] and the half-Heusler GdPtBi [21]. Recently, using magneto-terahertz spectroscopy (a non-contact method), Cheng and coworkers investigated epitaxial DSM $\mathrm{Cd_3As_2}$ films, in which the conductivities $\sigma(\omega)$ as a function of $\boldsymbol{\vec{E}}\cdot\boldsymbol{\vec{B}}$ showed a sharp Drude response over the background. This behavior was taken as a definitive signature of the chiral anomaly [22].

The chiral anomaly is a dynamic behavior of chiral fermions. In the absence of external fields, left-handed and right-handed fermions are present in the ground

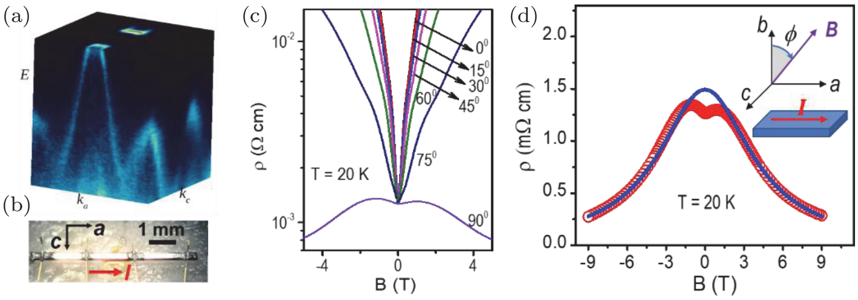

Fig. 2. (a) Angular resolved photoemission spectroscopy (ARPES) of a DSM $ZrTe_5$ showing linearly dispersed electronic bands near Fermi level. (b) Current-voltage configurations and a single crystal $ZrTe_5$ used for detecting the chiral magnetic effect, free of measurement artifacts, e.g., current-jetting. (c) Angular dependent longitudinal magnetoresistance (LMR) of $ZrTe_5$ at 20 K showing the negative LMR in parallel electric and magnetic fields (i.e. $\phi = 90°$). (d) A quadratic magnetic field dependence of negative LMR in parallel $\vec{E}$ and $\vec{B}$ fields – a characteristic property of the chiral anomaly in Weyl systems. (b-d from Ref. [12]).

state in equal numbers. There is no chiral current as expected for a system in thermodynamic equilibrium. Because of the anomaly, the chiral charge is not conserved, and can decay in the presence of parallel electric and magnetic fields. The chiral anomaly, sourced by non-zero $\vec{E} \cdot \vec{B}$, generates a non-zero chiral chemical potential difference that produces so-called charge pumping, shown in the left panel of Fig. 1d. The generation of this chiral current is the chiral magnetic effect. The chiral magnetic effect is not a thermodynamic phenomenon or ground state property. Its direct consequence is the large negative longitudinal magnetoresistance predicted by Nelson and Ninomiya. Notably, the chiral magnetic effect was previously misunderstood by some researchers as a thermodynamic phenomenon, where the associated chiral current was suggested to be proportional to the energy difference between the left-handed and right-handed Weyl nodes, rather than proportional to the chiral chemical potential difference (as it should be).

3. Topological phase transitions

The topological states in TIs and DSMs/WSMs are largely due to strong spin-orbit interactions. Lead chalcogenides Pb(Te, Se) are classic semiconductors that were extensively investigated for thermoelectric power generation in the 1950's. In 1966, a band inversion for $Pb_xSn_{1-x}Te$ alloys was reported [24]. The valence and conduction bands of SnTe are inverted from that of PbTe, with the band gap initially decreasing with rising Sn content, going to zero at an intermediate Sn content, then increasing again with rising Sn content [24]. The electronic band topology transforms from a trivial band insulator Pb(Te, Se) at one end to a non-trivial topological crystal insulator Sn(Te, Se) at the other end. A gapless DSM is at an intermediate Sn content [23]. Another example of composition controlled topological phase transition exists in $Bi_{1-x}Sb_x$. Elemental Bi is a classic semimetal,

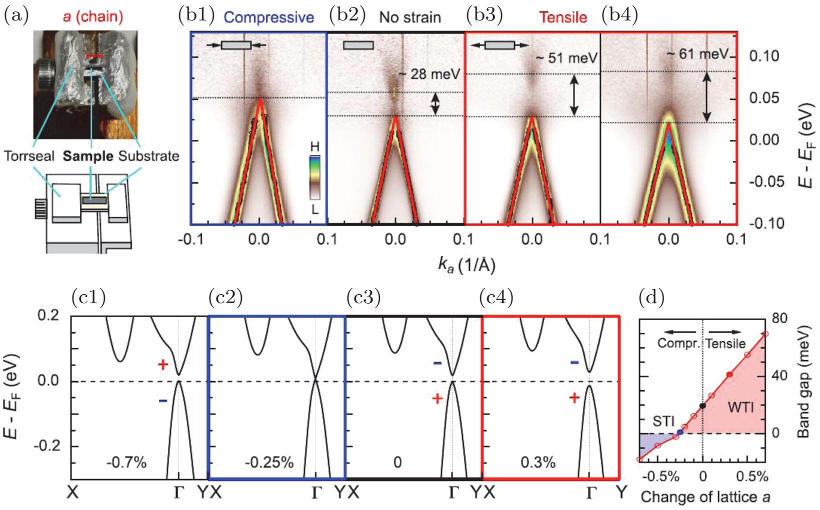

Fig. 3. Control of the topological phase in $ZrTe_5$ by external strain. (a) The strain device. (b) ARPES results: bulk band gap changes with compressive (Dirac state) and tensile strain (weak topological insulator). (c) The band structure calculations with different lattice constant a. + and − signs indicate the parity of the two bands. (b), (c) The blue (red) frames correspond to compressive (tensile) strain. (d) Calculated phase diagram with different lattice constant (strain). Solid markers roughly indicate the experimental values (from Ref. [25]).

and adding Sb (x in at. %) in $Bi_{1-x}Sb_x$ closes the band gap near $x \approx 3.5 - 6\%$. Alloys with $x > 8.6\%$ produce a direct-gap TI. A DSM emerges at a doping level in the range of 3.5 – 8.6 %.

The gapless Dirac points in DSMs are protected by time-reversal symmetry and crystal inversion symmetry. A small distortion in the crystal lattice can open a gap leading to DSM to TI transition [25, 26]. Taking $ZrTe_5$ as an example, Fig. 3 shows that a small amount of uniaxial strain can drive the material from a strong topological insulator (STI) to weak topological insulator (WTI) with a DSM in between [25]. Using laser-based angular resolved photoemission spectroscopy (ARPES), the topological states in ZrT_5 can be visualized under external strain. In this experiment, the uniaxial strain along the high conducting Te-chain direction was applied by using a screw to compress or stretch the substrate on which the single crystal sample was glued (Fig. 3a). With compressive strain, the gap was closed, reaching a DSM state. With tensile strain (Fig. 3b3–3b4), the band gap became larger, stabilizing the WTI state [25]. + and − signs in Fig. 3c1-3c4 indicate that the parity of the two bands are reversed in the STI and WTI phases. The example in Fig. 3 demonstrates the control of topological states via static strain. This control can also be achieved using a dynamic approach (e.g. Raman active phonons), which is described next.

We used first-principles methods to demonstrate that in $ZrTe_5$, atomic displacements corresponding to five of the six zone-center A_g (symmetry-preserving) phonon

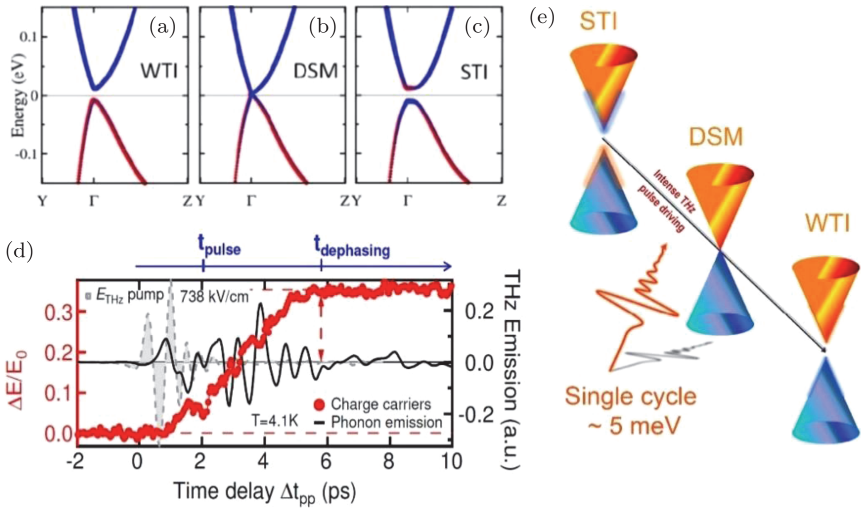

Fig. 4. (a)–(c) Evolution of the band structure and of the orbital content of the bands in $ZrTe_5$ forming the Dirac cone around the Γ point for different values of the normal coordinate Q corresponding to the A_g-27 Raman-active phonon mode. The Q values are (a) −0.6, (b) −0.25, and (c) 0.3. (d) THz differential transmission ($\Delta E/E_0$, red circles) as a function of the pump-probe time delay (Δt_{PP}) for a peak pump E field of 736 kV/cm. The black trace shows the simultaneously measured phonon emission. The THz-pump trace is shown in gray. The THz differential transmission starts to build up during the coherent phonon emission at much longer times than the pump THz pulse. (e) Schematic of the topological switching driven by the THz coherent excitation in Dirac semimetals. (a–c from Ref. [27], d–e from Ref. [28]).

modes can drive a topological phase transition from STI to WTI, with a DSM state emerging at the transition [27]. Shown in Fig. 4a–4c are the evolution of the band structure and orbital content of the bands in $ZrTe_5$ forming the Dirac cone around the Γ point for different values of the normal coordinate Q, corresponding to the A_g-27 Raman-active phonon mode. These topological phases in $ZrTe_5$ can be realized with many different settings of external stimuli that can penetrate through the phonon-space Dirac surface without breaking crystallographic symmetry.

In Fig. 4d, 4e, a few-cycle THz-pulse-induced topological phase transition in $ZrTe_5$ is depicted, driven by the lowest Raman active mode A_{1g} [28]. Above a critical THz-pump field threshold, a long-lived metastable phase of approximately 100 ps emerged. These results, taken together with first-principles modeling, identified a mode-selective Raman coupling that drives the system from STI to WTI, with a DSM phase established at a critical atomic displacement, controlled by the phonon coherent pumping. Harnessing vibrational coherence to steer symmetry-breaking transitions (i.e., Dirac to Weyl transitions) has implications for THz topological quantum gate and error correction applications in quantum information science and technology.

4. Chiral photocurrent and chiral qubits

While chiral current can be generated by a static magnetic field via the chiral magnetic effect, it can also be generated by electromagnetic waves. Circular polarized light (CPL) carries the left or right helicity of electromagnetic fields, which can couple to the chirality of charge carriers in Weyl semimetals. The current generated in the chiral fermionic system by the CPL, via circular photogalvanic effect, carries the chirality information of the system. This was the approach used by Q. Ma and collaborators to directly detect the chirality of the Weyl fermions in WSM TaAs by measuring chirality dependent photocurrent induced by circularly polarized mid-infrared light [29].

Chirality dependent photocurrent can also be generated in DSMs dynamically if its crystal inversion symmetry is broken, thus transforming DSMs to metastable WSMs. We used first-principles and effective Hamiltonian methods to show that in central-symmetric DSM $ZrTe_5$, lattice distortions corresponding to all three types of zone-center infrared (IR) optical phonon modes can drive the system from an STI or WTI to a WSM by breaking the global inversion symmetry [30]. Fig. 5a shows the "twisting" IR phonon mode B_{1u}-4 of $ZrTe_5$ projected onto the b − c plane, with the vectors indicating the normal atomic displacement. Such dynamic crystal

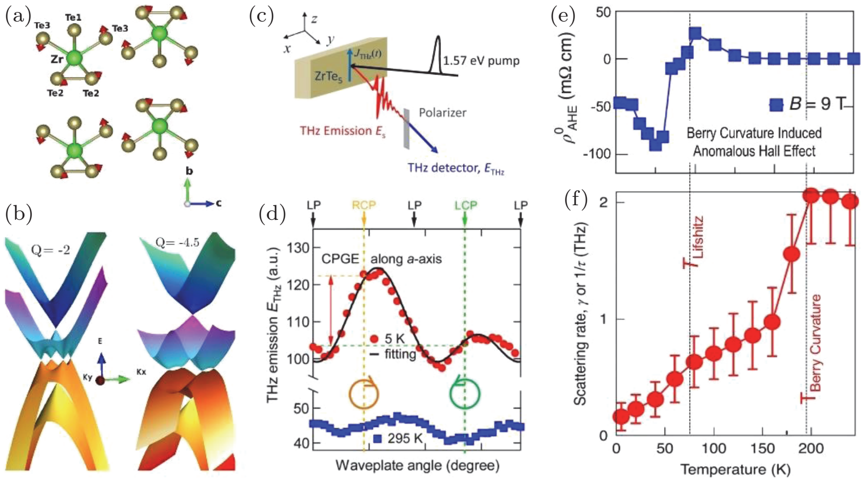

Fig. 5. (a) IR phonon mode B_{1u}-4 of $ZrTe_5$ projected onto the b−c plane with the vectors showing the normal atomic displacement. (b) Bands forming the Weyl points on the $k_x - k_y (k_a - k_b)$ plane for different Q values corresponding to the B_{1u}-4 phonon mode. (c) Experimental schematics for polarized THz emission spectroscopy to detect chiral photocurrent from THz fields E_s and E_{THz}. (d) Helicity dependent THz emission peak-to-peak amplitude along the a- axis, orthogonal to the light-induced symmetry-breaking axis, as a function of the quarter waveplate angle at 5 K and 295 K; 0, 90 and 180 degrees represent linear polarization (LP) of the pump; 45 and 135 degrees represent right (RCP) and left (LCP) circular polarization of the pump, respectively, and are marked on the top. (e) Temperature-dependent anomalous Hall saturation resistivity measured at 9 T. (f) Temperature-dependent chiral photocurrent scattering rate. (a–b from Ref. [30], c–f from Ref. [31])

"twisting" gives rise to electronic bands forming the Weyl points, shown in Fig. 5b. The achieved Weyl phases are robust, highly tunable and one of the cleanest Weyl systems due to the proximity of the Weyl points to the Fermi level [30].

Giant anisotropic THz photocurrents with vanishing scattering were discovered in $\mathrm{ZrTe_5}$ by using femto-second laser induced coherent phonons to break inversion symmetry [31]. The experimental schematics are shown in Fig. 5c. This light-induced phononic symmetry switching leads to formation of Weyl points, whose chirality manifests in a transverse and helicity-dependent photocurrent. This chiral photocurrent is orthogonal to the broken inversion symmetry axis, generated via the circular photogalvanic effect, shown in Fig. 5d. The chiral photocurrent has two distinct temperature–dependent features: i) Berry curvature creation by the separated Weyl nodes and strongly–suppressed scattering (Fig. 5f), with the same onset temperature $T_{\text{Berry curvature}}$, at which anomalous Hall resistivity was detected in the crystals (Fig. 5e) and ii) particle-hole reversal near the temperature-induced Lifshitz transition [32, 33]. Together with first-principles modeling, these results identify two pairs of Weyl points dynamically created by broken inversion-symmetry phonons of the $\mathrm{B_{1u}}$ mode, which are driven by the photoexcited and non-equilibrium population of spatially separated charges between the inverted bands of the Te pair. The chiral current appears dissipationless towards low temperature as the scattering rate of photocurrent (Fig. 5f) approaches zero. Berry curvature dominance below $T_{\text{Berry curvature}}$ marks the sharp suppression of the scattering rate. In addition to revealing dissipationless photocurrents with remarkable ballistic chiral fermion transport lengths of $\sim 10\,\mu$m, the phononic symmetry switching principle lays the groundwork for the coherent manipulation of Weyl states without application of any static electric or magnetic fields.

In the absence of chirality flipping, the chiral anomaly produces a flow of dissipation-free charge, which is useful for electronics and optoelectronics requiring ultralow energy consumption. Chiral photocurrents offer a new type of light-electricity conversion device, which we termed a chiral photovoltaic cell, depicted in Fig. 1e. This device converts light into electricity using a set of optical lenses and does not suffer from the electron-hole recombination process that limits conversion efficiency in a conventional solar cell with semiconductor p-n junctions.

Chiral materials make good candidates for topological qubits and quantum transducers, because of the chiral current and its ability to couple the helicity (CPL) of an electromagnetic field to the chirality of charge. This is depicted in Fig. 1c and Fig. 1f, respectively. The chiral qubit [33] we proposed is enabled by the chiral anomaly and constructed from a micron-meter-scale ring made of a WSM. The $|0\rangle$ and $|1\rangle$ states correspond to the symmetric and antisymmetric superpositions of quantum states describing chiral fermions circulating along the ring clockwise and counter-clockwise. The entanglement of qubits can be implemented through the application of a circularly-polarized THz frequency electromagnetic wave to the system. Chiral qubits are advantageous because they can be potentially operated at room temperature, at THz frequencies, and with a large ratio of the coherence to gate time on the order of 10^4.

In quantum communication applications, chirality can function as an encoder and a decoder for a transmitted message, as well as a "quantum bus" between devices operating at different frequencies. Examples include GHz superconducting qubits and optical communication channels. A chiral photocurrent-based transducer would be revolutionary as it could have the capabilities of generation, transduction (high fidelity down-conversion and up-conversion), and coherent control of the photon polarization at GHz to UV frequency ranges. This can be achieved using chirality, which is intrinsic to the chiral fermions in 3D DSMs/WSMs, without invoking traditional methods such as waveplates, polarizers, or low-efficiency nonlinear crystals.

In conclusion, the powerful notion of chirality, originally discovered in high energy and nuclear physics, underpins a wide range of new phenomena and useful applications. Recent discoveries of the chiral anomaly in a variety of materials have made it possible to study the quantum dynamics of relativistic field theory in condensed matters. The observation of chiral anomaly-enabled photocurrent generation opens a new avenue for novel electronics requiring ultra-low-energy dissipation that we call "chiraltronics". The potential of chiraltronics may be further enhanced by our abilities to statically and dynamically control the topological phase transitions between TIs and DSMs/WSMs. The proposed exploration of chiral qubits and chiral transduction may help to answer a grand challenge underlying the field of topology-enabled quantum information science and technology: how to establish principles of topological control, driven by quantum coherence, and understand its time-dependent effects. The advances described in this article make the "dynamics of chiral fermions in condensed matter systems" an exciting and potentially transformative field.

Acknowledgments

The author would like to express his sincere gratitude for Prof. Dmitri Kharzeev for generously giving of his knowledge in chiral magnetic effect, and many fruitful collaborations. The author would also like to acknowledge collaborations with Drs. Cheng Zhang, Genda Gu, Tonica Valla, Jigang Wang, and Mengkun Liu.

References

1. A. K. Geim, "Graphene: Status and Prospects" *Science* **324**, 1530 (2009).
2. A. K. Geim and K. S. Novoselov, "The rise of graphene" *Nat. Mater.* **6**, 183 (2007).
3. A. H. Castro Neto, F. Guinea, N. M. R. Peres, K. S. Novoselov, and A. K. Geim "The electronic properties of graphene" *Rev. Mod. Phys.* **81**, 109 (2009).
4. M. Z. Hasan and C. L. Kane " Colloquium: Topological insulators" *Rev. Mod. Phys.* **82**, 3045 (2010).
5. X. L. Qi and S. C. Zhang, "Topological insulators and superconductors" *Rev. Mod. Phys.* **83**, 1057 (2011).

6. Z. Wang, *et al.* “Dirac semimetal and topological phase transitions in $A_3Bi\,(A =$ Na, K, Rb$)$”. *Phys. Rev. B*, **85**, 195320 (2012).
7. Z. Wang, *et al.* “Three-dimensional Dirac semimetal and quantum transport in Ca_3As_2” *Phys. Rev. B*, **88**, 125427 (2013).
8. S. M. Young, *et al.* “Dirac semimetal in three Dimensions” *Phys. Rev. Lett.* **108**, 140405 (2012).
9. B. Yang and N. Nagaosa “Classification of stable three-dimensional Dirac semimetals with nontrivial topology” *Nature Communications* **5**, 4898 (2014).
10. S. Xu, *et al.* “Discovery of a Weyl fermion semimetal and topological Fermi arcs” *Science* 349, 613–617 (2015).
11. B. Q. Lv. *et al.* “Experimental discovery of Weyl semimetal TaAs” *Phys. Rev. X* **5**, 031013 (2015).
12. Q. Li, *et al.* “Chiral magnetic effect in $ZrTe_5$” arXive:1412.6542 (2014), *Nature Physics* **12**, 550 (2016).
13. D. Kharzeev and Q. Li “Quantum computing using chiral qubits” US Patent #10,657,456 (2020); D. Kharzeev and Q. Li “The Chiral Qubit: quantum computing with chiral anomaly” arXiv:1903.07133.
14. S. L. Adler, “Axial-vector vertex in spinor electrodynamics” *Phys. Rev.*, **177**, 2426 (1969).
15. J. S. Bell and R. Jackiw “A PCAC puzzle: $\pi^{o} \rightarrow \gamma\gamma$ in the σ-model” *Il Nuovo Cimento* A, **60**, 47–61 (1969).
16. H. B. Nielsen and M. Ninomiya. “The Adler-Bell-Jackiw anomaly and Weyl fermions in a crystal” *Physics Letters* B, **130**, 389–396 (1983).
17. K. Fukushima, D. Kharzeev, and H. Warringa. “Chiral magnetic effect” *Phys. Rev. D*, **78**, 074033 (2008); D. E. Kharzeev “The chiral magnetic effect and anomaly-induced transport” *Progress in Particle and Nuclear Physics*, **75**, 133–51 (2014); D. Kharzeev “Parity violation in hot QCD: Why it can happen, and how to look for it”. *Physics Letters* B, **633**, 260–264 (2006).
18. D. E. Kharzeev and J. Liao, “Chiral magnetic effect reveals the topology of gauge fields in heavy-ion collisions” *Nature Reviews Physics* **3**, 55 (2021).
19. N. P. Ong and S. Liang “Experimental signatures of the chiral anomaly in Dirac–Weyl semimetals” *Nature Reviews Physics* **3**, 394 (2021).
20. F. Arnold, *et al.* “Negative magnetoresistance without well-defined chirality in the Weyl semimetal TaP” *Nat. Communications* **7**, 11615 (2016).
21. M. Hirschberger, *et al.* “The chiral anomaly and thermopower of Weyl fermions in the half-Heusler GdPtBi” *Nature Materials* **15**, 1161 (2016).
22. B. Cheng, *et al.* “Probing charge pumping and relaxation of the chiral anomaly in a Dirac semimetal” Science Advances, abg0914 (2021).
23. Q. Li “Thermoelectrics with a twist” *Nature Materials* **18**, 1267 (2019).
24. J. O. Dimmock, I. Melngailis, and A. J. Strauss “Band structure and laser action in $Pb_xSn_{1-x}Te$”. *Phys. Rev. Lett.* **16**, 1193–1196 (1966).
25. P. Zhang, *et al.* “Observation and control of the weak topological insulator state in $ZrTe_5$” Nature Communications **12**, 406 (2021).
26. J. Mutch, *et al.* “Evidence for a strain-tuned topological phase transition in $ZrTe_5$” Science Advances eaav9771 (2019).
27. N. Aryal, *et al.* “Topological phase transition and phonon-space Dirac topology surfaces in $ZrTe_5$” *Phys. Rev. Lett.* **126**, 016401 (2021).
28. C Vaswani, *et al.* “Light-driven Raman coherence as a nonthermal route to ultrafast topology switching in a Dirac semimetal” *Phys. Rev. X* **10**, 021013 (2020).

29. Q. Ma, *et al.* "Direct optical detection of Weyl fermion chirality in a topological semimetal" *Nature Physics* **13**, 842 (2017).
30. N. Aryal, *et al.* "Robust and tunable Weyl phases by coherent infrared phonons in ZrTe_5" *npj Comput Mater* **8**, 113 (2022).
31. L. Luo, *et al.* "A light-induced phononic symmetry switch and giant dissipationless topological photocurrent in ZrTe_5. *Nature Materials* **20**, 329 (2021).
32. H. Chi, *et al.* "Lifshitz transition mediated electronic transport anomaly in bulk ZrTe_5" *New J. Phys.* **19**, 015005 (2017).
33. P. Lozano, *et al.* "Anomalous Hall effect at the Lifshitz transition in ZrTe_5" *Phys. Rev. B*, **106**, L081124 (2022).